PROCEEDINGS, 48th Workshop on Geothermal Reservoir Engineering
Stanford University, Stanford, California, February 6-8, 2023
SGP-TR-224

Haskell Waveform Modeling of EGS Stimulation Meqs as Slow Ruptures Within Ambient Crust Permeability Structures

Peter Malin and Peter Leary

Advanced Seismic Instrumentation and Research

pem@asirseismic.com pcl@asirseismic.com

Keywords: Ambient crust, Meqs, EGS, poro-permeability, fluid injection, crustal stimulation, Haskell elastodynamics

ABSTRACT

We examine hHz displacement waveforms of microseismic (Meq) emissions induced by controlled fluid injection into crystalline basement at six km depth and recorded at 2kHz sample rate by vector seismic sensors at 2.5km depth above the stimulation volume. The hHz displacement waveforms for notional magnitude $0 < m < 1$ Meqs are bidirectional, inconsistent with the standard unidirectional Haskell fault-zone-like planar slip distributions. While the hHz waveforms are dominated by scattering (up to four-second coda wavefields), there is little wavefield amplitude degradation ($Q_{absorb} \sim 3000$). We can thus interpret the unscattered lead 10-20ms P-wave displacement wavefields in terms of Haskell-like source emission distributions commensurate with the ambient crustal rock-fluid interactions activated by fluid injection. Our waveform interpretation is validated by statistical commonality between the size/spatial correlations of the observed stimulation Meqs and the ambient crust poro-permeability empiric $\kappa(x,y,z) \sim \exp(\alpha\varphi(x,y,z))$; both stimulation Meqs and $\kappa(x,y,z)$ are lognormally distributed and spatially correlated via two-point correlation function $G(r) \sim 1/r$, r = site-pair/Meq-pair offset. The observed hHz bidirectional quasi-sinusoid P-wave first motion displacement waveforms are generically replicated by taking Haskell's elastodynamic integral over radially directed source-slip emissions within over-pressured volumetric permeability structures. Far-field Meq hHz bidirectional displacement sensor waveforms arise from summing over radially expanding distributions of slip velocity, with onset sensor arrivals emitted by radial slip towards sensors at slip sites nearer the sensor that are followed by later-arriving reversed-sign displacements from radial slip away from sensors emitted by sites further from the sensors. Hypothetically, EGS stimulation of the ambient crust proceeds via high-pressure fluid breakouts causing slip dislocations that increase the poro-connectivity parameter α in the $\kappa(x,y,z) \sim \exp(\alpha\varphi(x,y,z)$ ambient crust poro-permeability empiric. Permeability stimulation via increased α is energy efficient as fluid injection energy released through increased poro-connectivity does less work against crustal confining stresses. As fluid-induced poro-connectivity changes are systematically localised throughout spatially erratic ambient crust poro-permeability structures, EGS stimulation must be monitored by seismic-emission flow-structure imaging to locate permeability enhancement relative to service wellbores.

1. INTRODUCTION

A seminal result of modern seismology showed that seismic displacement waveforms emitted by fault-zone earthquakes can be attributed to coherent mechanical shear-slip dislocation fronts propagating along planar fault-like surfaces in an elastic crust (Haskell 1969; Aki & Richards 1980, 2009; Lay & Wallace 1995). While large-scale shear dislocation slip mechanics along active planar faults were long evident from field observation, it required a rigorous solution to the elastodynamics of incremental shear-slip to quantify the seismic wavefields recorded by seismometers. Haskell (1969) gave such an expression relating far-field fault-zone seismic displacement waveforms to summations over infinitesimal shear-slip velocity distributions that progress uniformly along planar structures (i.e., faults) at a fixed rupture velocity for finite durations $t_0 < t < t_1$. But unidirectional planar fault-zone shear-slip distributions at fixed rupture speed are only one realisation of the Haskell spatial integral. Here we use Haskell-like slip summation over radially expanding volumetric surfaces rather than along planar surfaces to describe a new/bidirectional class of microseismic (Meq) displacement waveforms recorded for controlled EGS stimulation of deep crustal basement [Kwiatek et al 2019].

To introduce Haskell summation displacement waveforms, Figure 1 compares the standard fault-zone-like daHz-frequency unidirectional "boxcar" displacement waveforms at left with observed hHz Meq bidirectional displacement waveforms in red at right. Making up the difference between left and right displacement waveforms requires a new class of Haskell-like spatial integration over distributions of radial slip dislocation velocities commensurate with the rock-fluid interaction properties that control the spatial distribution of EGS fluid injected into the volumetric permeability structures of the ambient crust.

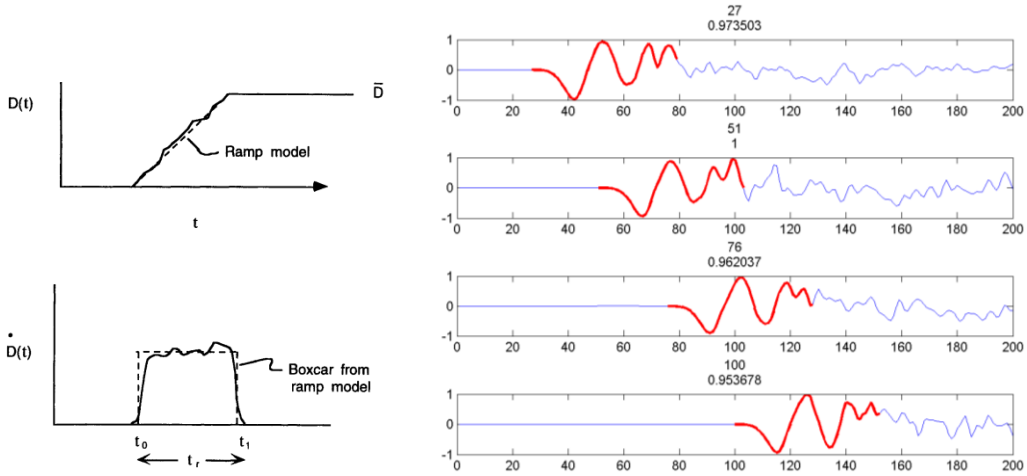

Figure 1: (Left) Fault-zone slip-mechanics constant velocity rupture dislocation profile (above) and resultant unidirectional far-field displacement waveform of duration t (below) (e.g., Lay & Wallace 1995). (Right) First motion P-wave displacement waveforms in red recorded at 2kHz sample rate on the Geospace GeoRes DW150 vertical axial array sensors in crystalline basement at 2.5km depth directly above a km-scale EGS controlled-stimulation volume at 6km depth (Kwiatek et al 2019). The Meq waveforms in ½ msec increments have peak frequencies ~400Hz for an event of notional moment-magnitude m ~0; nominal fault-events of this magnitude have corner-frequencies f_0 ~ 100Hz, equivalent to pictured boxcar waveform duration t ~ 10ms.

The essential components of Haskell integration can be stated for a far-field component u(r,t) of vector displacement generated by summing over (potentially spatially erratic) distributions of discretised slip dislocation velocity elements $\dot{D}_{ijk}$ of unit volumetric scale δV for spatial indices i,j,k running over the stimulation volume,

$$u(r,t) = \sum_{ijk} A_{ijk}\dot{D}_{ijk}(t-r_{ijk}/v)\ \delta V. \qquad (1)$$

In (1) r_{iik} is the distance from the i,j,k emission site to the far-field sensor, and A_{iik} is an amplitude factor specific to site i,j,k. The far-field seismic sensor displacement u(r,t) at sensor time interval $t \rightarrow t+dt$ at mean distance r from a discretised stimulation volume is fixed by source volume slip activity at earlier times. In a medium of seismic wave speed v, the relevant emissions from source slip dislocation velocities $\dot{D}_{iik}$ at spatial sites i,j,k occur in the time interval $t - r_{iik}/v \rightarrow t+dt - r_{iik}/v$. A_{iik} denotes physical factors including elastodynamic radiation patterns of the variously oriented point-source emitters at spatial locations i,j,k. With our far-field condition (mean source-sensor distance r ~ 4km >> ~ the 30-100m nominal dimension of the stimulated source emission volumes), small variations in r_{iik} from the mean distance r can be ignored and spatially erratic angular variations in source-slip motion and source-slip location for A_{ijk} can be averaged over to give an effective mean value A,

$$u(r,t) \sim A \sum_{ijk} \dot{D}_{ijk}(t-r_{ijk}/v)\ \delta V. \qquad (2)$$

Evaluating Haskell (2) requires fixing the times t in which emission elements $\dot{D}_{iik}(t-r_{iik}/v)$ are non-zero, i.e., specifying source motion at each given site i,j,k. For Haskell's fault-zone slip motion, $\dot{D}_{iik}(t-r_{iik}/v)$ is non-zero at times corresponding to the motion of the fault-zone rupture front moving across site i,j,k. For our present purposes, $\dot{D}_{iik}(t-r_{iik}/v)$ is non-zero at times when radial fluxes of high pressure fluid pass through volume elements i,j,k within a localised poro-permeability structure given by the ambient crust poro-permeability distribution $\kappa(x,y,z) \sim \exp(\alpha\varphi(x,y,z)$ reviewed in Appendix A.

Applying Haskell (2) to Figure 1, the contrast between the standard planar coherent fault-zone slip mechanics (left) and our Meq displacement waveforms u(r,t) in red (right) implies summing over a range of radial slip velocities $\dot{D}_{iik}(t-r_{iik}/v)$ in the direction of the sensor, followed within ~ 5-10 ms by reverse sign radial slip velocities from sites away from the sensors. The observed hHz bidirectional sinusoidal displacement waveforms can thus logically proceed from sums over discrete units of radial slip distributed within localised ambient crust permeability structures that have been steadily over-pressured by controlled wellbore EGS fluid injection.

Fixing the times t in which $\dot{D}_{iik}(t-r_{iik}/v)$ is non-zero is equivalent to a mathematical inversion process that seeks to match the Haskell integral (2) to observed far-field displacement waveforms u(r,t). We formulate our "inversion" of EGS stimulation of Meq P-wave first motion in simplified terms of Stokes' relation for P-wave displacement $u_n(\mathbf{x},t)$ at far-field location $\mathbf{x}$ due to point-force F_P at source volume location ξ as given by Aki & Richards (2009, Eq 4.27),

$$u_n(\mathbf{x},t) \propto \gamma_n\gamma_P F_P(t - r/\alpha),\ r = |\mathbf{x}-\xi|,\ \gamma_n = (x_n - \xi_n)/r, \qquad (3)$$

where force F_P is notionally taken to be on average radially-directed by the outward flux of pressurised fluid within localised ambient crust poro-permeability structures $\kappa(x,y,z) \sim \exp(\alpha\varphi(x,y,z)$.

Because the amplitude of the radial forces within the deflating permeability structure are unknown (and unknowable), our inversion scheme omits the Stokes pre-factor $1/(4\pi\rho\alpha^2)/r$ of Aki & Richards (2009). While the geometric simplicity of fault-zone planar shear-slip

distributions allowed Haskell to engage in detailed amplitude simulations, our present interest is restricted to the temporal shape of the Stokes displacement waveform point representation (3) as summed over temporally/radially-defined source emission surfaces.

2. ELEMENTS OF HASKELL DISPLACEMENT WAVEFORM SPATIAL INTEGRATION FOR FAULT-ZONE MEQS

The validity of our displacement waveform modelling is based on the Haskell integral (2) applied to Figure 1 (left) that has long been observed to closely agree with the slip mechanics of active faulting (Aki & Richards 2009). The spatial coherence of the standard source of Haskell shear-slip velocity distributions $\dot{D}_{ijk}$ leads to destructive interference of seismic wavelengths smaller than the characteristic dimension L of the slip plane. With internal seismic wavefield interference acting as a frequency filter of forms like $F(f) \sim 1/(1+(f/f_0)^2)$, a "corner frequency" f_0 scales inversely with fault dimension, $f_0 \sim 1/L$. As event moment/magnitude scale with L^3, the multi-decadal scaling data of Appendix B restricts fault-zone-like Meqs of magnitudes $0 < m < 1$ to daHz corner frequencies below the hHz frequencies of the Figure 1 stimulation Meq waveform frequencies. Appendix B further fixes fault-zone-like shear-slip event Meq stress drops at order $\Delta\sigma \sim 1$MPa. Breaking down fault-zone slip mechanics into Haskell (2) units gives a notional measure of a unit Haskell shear-slip process energies that can be conceptually applied to volumetric source distributions of present interest. Unit Haskell slip events have energies given by stress drop $\Delta\sigma \sim 1$MPa as $E \sim \Delta\sigma/G \times M$ for slip of seismic moment M in elastic media of rigidity G (e.g., Venkataraman & Kanamori 2004).

Further to volumetric Haskell integrals, details of applying Haskell (2) to fault-zone Meq displacement waveforms are sketched in Figure 2.

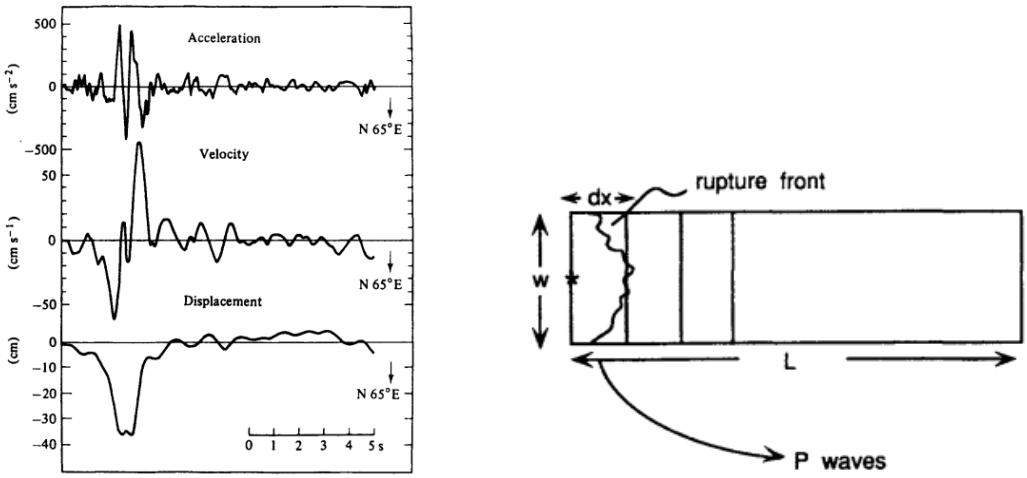

Figure 2: (Left) San Andreas fault-zone earthquake sensor data for 1966 Parkfield event (Aki 1968; Aki & Richards 2009); integrating the top acceleration data twice gives the far-field unidirectional boxcar displacement waveform at the bottom. (Right) A fault-zone slip event in vertical section time sequence for uniform slip over fault height W and uniform rupture velocity v_r in discrete time steps $dt = dx/v_r$ along fault length L (e.g., Lay & Wallace 1995).

In Figure 2 (left) the 1966 San Andreas fault earthquake at Parkfield CA generated ground motion accelerations at the top. Ground accelerations integrated once gives sensor velocity motion, and integrated twice register ground displacements. In accord with the Haskell fault-slip process of Figure 1 (left), the observed ground displacement takes a unidirectional boxcar form when the fault rupture sequence proceeds as sketched in Figure 2 (right).

In terms of fault geometry and slip event size/moment, a dislocation front of shear-slip amplitude Δ and height W progresses from left to right along the fault length L at steady rupture speed v_r in displacement increments $dx = v_r dt$ in time increments dt. Nominal constant slip velocities are close to the shear-wave velocity of the embedding rock volume, $v_S \sim \sqrt{G/\rho}$ fixed by the elastic rigidity G and mass density ρ of the rock volume. The energy scale of the slip event follows from these parameters as the earthquake moment $M = \Delta AG$, for $A = WL$ the area of the total slip surface. Haskell (2) for a single spatial index gives the far-field elastic displacements of Figures 1-2 (left) created by the rupture front of Figure 2 as the sum over instantaneous shear-slip displacements dx of height W for $n = L/dx$ time increments $i \cdot dx/v_r$,

$$u(r,t) \propto \sum_{i=1:n} \dot{D}_i(t - r/v - i \cdot \delta x/v_r). \qquad (4)$$

It follows from (4) for constant incremental element displacement velocity $\dot{D}_i = \dot{D}_0$ that the far field displacement is zero at times before the slip begins at t_0 and after the slip stops at time t_1, and is constant at all intermediate time steps $t_0 < i \cdot dx/v_r < t_1$, $i = 1 \ldots n$. This model produces the Figure 1 boxcar waveform in accord with the Figure 2 observed sensor motion for the Parkfield 1966 earthquake. Lay and Wallace (1995) enlarge on fault-zone EQ waveform modelling; more detailed mathematical treatments are given by Madariaga (1976; 1977; 1979); a global earthquake first motion catalogue attests unidirectional fault-zone source processes (Vallée & Douet 2016).

In defaulting from the unidirectional boxcar waveform, the Figure 1 EGS Meq displacement waveforms effectively dismiss notional quasi-faulting for controlled EGS stimulation in the ambient crust (i.e., away from active fault zones as in Kwiatek et al 2019). Appendix C

details the very considerable deviation of our EGS stimulation Meqs from the spatial statistics of standard fault-zone-like shear-slip events. Through the generality and simplicity of Haskell (2), we supplant the defaulted Figure 2 fault-like shear-slip source distributions with alternative shear-slip source distributions that replicate Figure 1 observed EGS Meq displacement waveforms. It is logical to base trial Stokes slip dislocation velocity distributions $\dot{D}_{ijk} \sim F_p$ on localised volumes of over-pressured fluid collected within spatially-correlated random poro-permeability structures $\kappa(x,y,z) \sim \exp(\alpha\varphi(x,y,z)$ discussed in Appendices A and C.

3. HASKELL DISPLACEMENT WAVEFORM SPATIAL INTEGRATION OVER AMBIENT CRUST PORO-PERMEABILITY VOLUMES

It is evident from Appendix C that EGS stimulation Meq spatial correlation statistics that injected fluids act within pre-existing localised volumetric ambient crust permeability structures $\kappa \sim \exp(\alpha\varphi)$. It is further logical that static fluid pressure gradients and consequent fluid pressure relief displacement motions are essentially radial within localised ambient crust permeability structures. Figures 3-5 illustrate that the spatial correlation features of UtahForge ambient crust EGS stimulation Meqs recorded by surface sensors also engage with the empirical ambient crust permeability structure $\kappa(x,y,z) \sim \exp(\alpha\varphi(x,y,z)$. The spatially correlated porosity distributions lead to the lognormally distributed permeability magnitudes that are matched to Stage 1-3 UtahForge Meq magnitude distributions. The Meq emission pressure release mechanics are logically rapid versions of the slow rock compaction processes that produce the ambient crust permeability structure empiric $\kappa(x,y,z) \sim \exp(\alpha\varphi(x,y,z))$ detailed in Appendix A. Figure 4 displays the inherent spatial correlation of regions of high poro-permeability localities within a 512x512x512 numerical realisation of $\kappa(x,y,z) \sim \exp(\alpha\varphi(x,y,z)$. Figure 5 compares the two-point spatial correlation function $G(r) \sim 1/r^p$, $p \sim 1$, numerically realised in Figure 4 with that of the three stages of UtahForge stimulation Meqs.

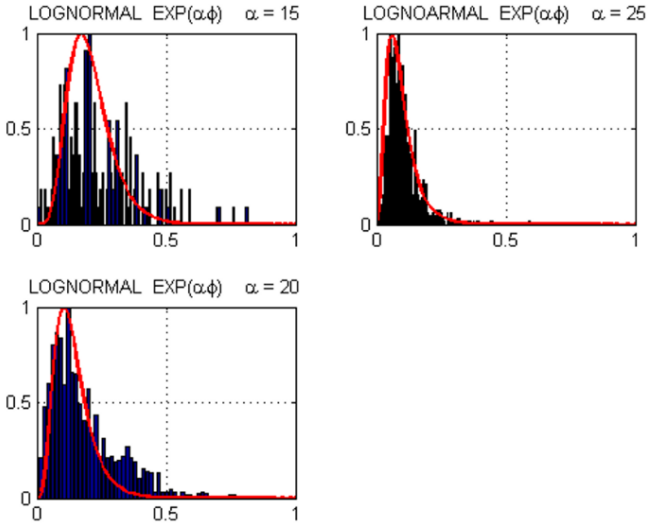

Figure 3: Lognormal UtahForge 2022 EGS stimulation event size distributions using of $\kappa(x,y,z) \sim \exp(\varphi(x,y,z)$ as a function of poro-connectivity parameter α; the lognormal curve refutes the standard Gutenberg-Richter distribution validated in active fault zones but not observed in ambient crust.

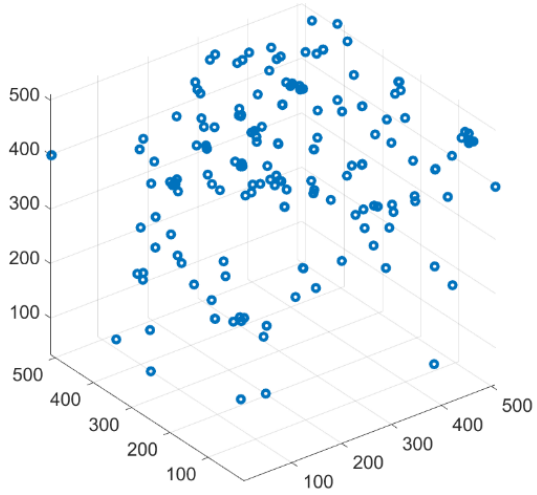

Figure 4: Spatial clustering of 300 highest poro-perm values of numerical realisation of $\kappa(x,y,z) \sim \exp(\varphi(x,y,z))$ for $\alpha = 25$ as mandated by Figure 3. The cluster scale sizes indicate the notional dimension of local high-value poro-perm loci that are logical candidates for Meq shear-slip distributions modelled by Haskell spatial integration (4).

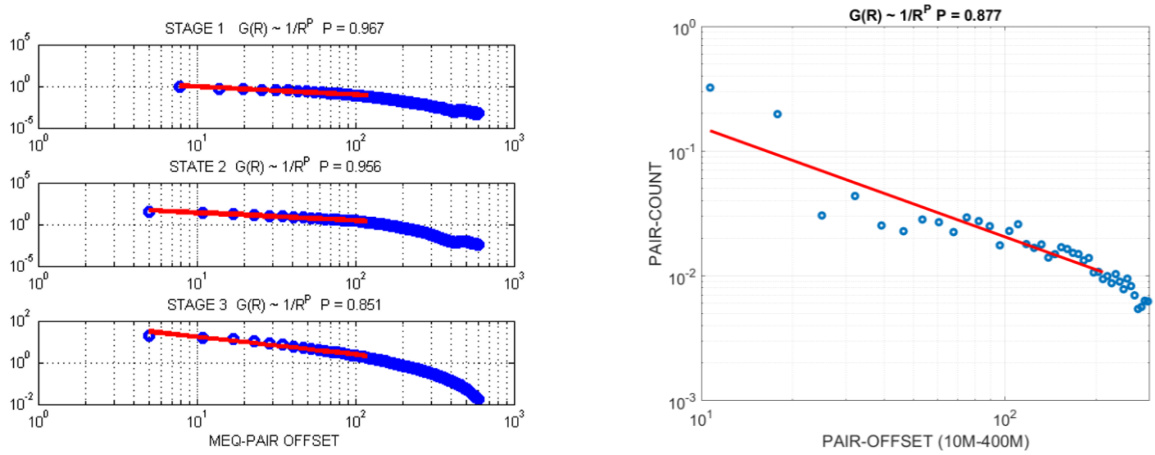

Figure 5: Two-point spatial correlation function $G(r) \sim 1/r^p$, $p \sim 1$, for UtahForge stage 1-3 stimulation Meqs (left) and for spatial clustering of Figure 4 high-value poro-perm distributions of $\kappa(x,y,z) \sim \exp(\varphi(x,y,z))$, $\alpha = 25$ (right). In both field and numerical cases, the spatial correlation exponent is $p \sim 1$ for an event-pair offset scale range ~ 30.

As we are presently unable to assign plausible magnitudes to Haskell radial slip dislocation unit velocities, we have no constraints on the Haskell summation over nominal surfaces represented by plausible geometric shapes. We thus approach evaluating the Haskell integral in terms of geometric shapes embedded within a numerical volume of m-scale cubes that are organised on three length scales. At the m-scale, each elementary cube is taken to have a mean permeability distributed as $\kappa(x,y,z) \sim \exp(\alpha\varphi(x,y,z))$. The m-scale elementary cube permeabilities are then numerically represented by nodes within a km-scale crustal volume with m-scale values distributed according to the essentially universal ambient crust poro-permeability empiric $\kappa_{IJK} \sim \exp(\alpha\varphi_{IJK})$, I,J,K ~ 1:500. As illustrated by Figure 4, within the km-scale are individual sites of high local permeability that act as local repositories of high-pressure fluid subject to sudden breakout. Each such local repository of high fluid pressure comprises some thousands of elementary cubes. Local intermediate-scale high poro-connectivity/permeability sub-structures denominated by $\kappa_{ijk} \sim \exp(\alpha\varphi_{ijk})$, ijk ~ 1:50, are the focus of our ensuing Haskell summations that generate the far-field numerical displacement waveform models for EGS stimulation hHz far-field Meq data.

In the face of spatial complexity within localised pressured poro-permeability structures, we may organise the Haskell summation by approximating the Meq pressure-release sequence by a succession of ellipsoidal envelopes within the permeability structure. The simplest ellipsoid is a sphere, but such spatial uniformity does not square with either the spatial properties of the crustal permeability field $\kappa_{ijk} \sim \exp(\alpha\varphi_{ijk})$ or the observed variety of Meq displacement first motion waveforms. Proceeding with ellipsoidal Haskell integration volumes, we can take the effective local radius of fluid pressure release to be the normal to the ellipsoid surface at any given point within the $\kappa_{ijk} \sim \exp(\alpha\varphi_{ijk})$ ensemble. The effect of such net shear-slip dislocation motion on the far field displacement sensor is a function of the direction of the motions within the aligned vertical dislocation plane relative to the direction of the source volume to the sensor. Statistically, the direction of shear-slip dislocation motion is logically biased towards the radial direction. In this approximation, the Haskell slip dislocation motion is computed for each normal to the surface of the enclosing ellipsoid representing the Stokes point force given by (3). The resulting

Haskell summation is thus a product of the ellipsoid dimensions and axis orientation with allowance for a sequence of expanding ellipsoids that grow radially by a nominal rupture-front velocity.

Figure 6 illustrates the numerical realisation of far-field displacement waveforms generated by Haskell integration over unidirectional planar shapes (left) and bidirectional ellipsoidal shapes (right).

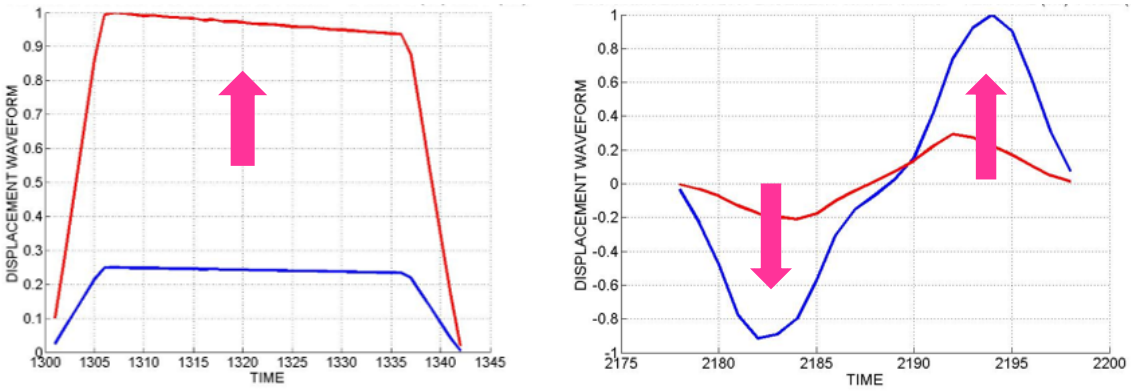

Figure 6: (Left) Unidirectional far-field P-wave displacement waveform for Haskell shear-slip on fault-zone planar surface as documented for Parkfield 1966 earthquake on San Andreas fault displayed in Figure 2 and Figures 10.17-18, Aki & Richards (2009). (Right) Bidirectional far-field P-wave displacement waveform for Haskell radial slip normal to ellipsoid-surfaces embedded in poro-permeability structures given by ambient crust poro-permeability empiric $\kappa(x,y,z) \sim \exp(\alpha\varphi(x,y,z))$ as illustrated as poro-permeability clusters in Figure 4.

Figure 7 illustrates Haskell-based evaluations (2) of far-field P-wave displacement motion for summation over radially-directed Stokes forces (3) for sequences of ellipsoidal rupture front surfaces expanding at an intermediate rate. Representative ellipsoidal surfaces are shown in Figure 8. The Haskell waveforms in red are superposed on six representative Meq far-field P-wave first-motion displacement waveforms in blue. The Meqs of nominal magnitudes $0 < m < 0.5$ occurred over a 4-hour period during controlled stimulation of crystalline basement as described by Kwiatek et al (2019). No exceptions to the Figure 7 waveform format have been observed for several hundred stimulation Meqs across nominal a magnitude range $-0.5 < m < 1.5$.

The essential contents of Figures 7-8 are (i) clear absence of the unidirectional far-field displacement waveforms illustrated at the left of Figures 1,2 and 6, (ii) consistent presence of balanced bidirectional displacement waveforms as observed in Figure 1 (right) and modelled in Figure 6 (right), and (iii) ability to ascribe bidirectional first motion waveforms to seismic source emission volumetric distributions that are consistent with poro-permeability structures given by the $\kappa(x,y,z) \sim \exp(\alpha\varphi(x,y,z))$ empiric attested throughout the ambient crust. Figures 7-8 thus represent a new class of crustal Meq processes with the same clarity of evidence and consistency of mechanics that has been achieved for fault-zone seismology.

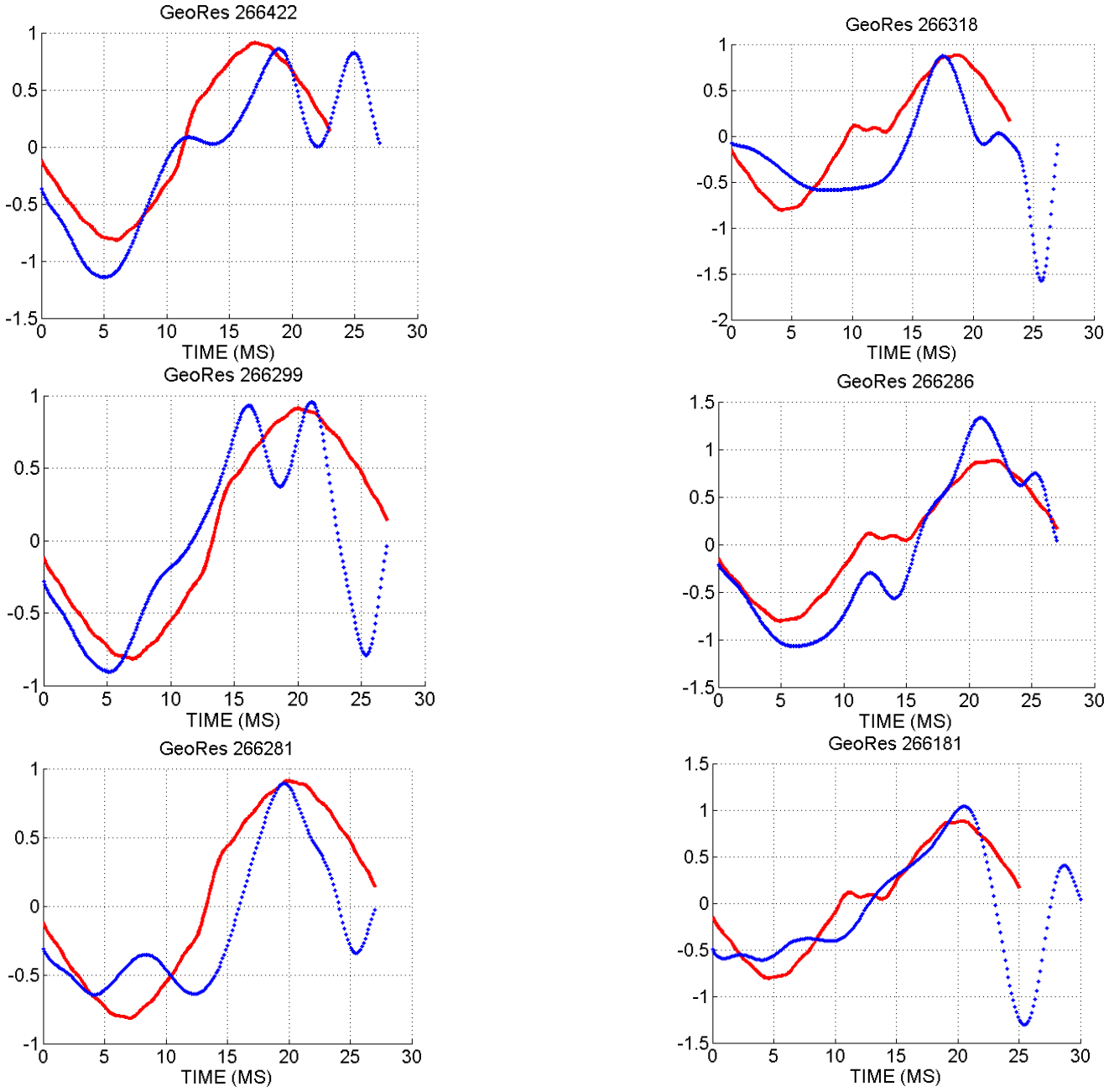

Figure 7: (Blue) Far-field P-wave first motion displacement waveforms for six stimulation Meqs induced in ambient crust basement by controlled fluid injection at six km depth; events occurred over a 4-hour interval at times given by the recording minute in plot titles. (Red) Displacement waveforms computed for Stokes far-field P-wave displacement (4) summed over radial emissions for a sequence of outward expanding ellipsoids at intermediate rupture velocity.

The scale of the Figure 8 ellipsoids is determined by the characteristic time-scale of the displacement waveform. The $\tau \sim 20$ ms waveform duration is given jointly by the difference between first and last far-field emission arrivals from the source volume, and by the speed of the fluid rupture front as the over-pressured poro-permeability structure releases its fluid in a succession of ellipsoidal surfaces. The major dimension of the Figure 8 ellipsoids is nominal 70 m and the rupture speed of successive ellipsoids is a nominal one half of the shear-wave velocity of the crust. The more elongate ellipsoids labelled 5,6,9 provide the closer fits to Meq waveforms, nominally indicating that the source distribution is more nearly lateral than symmetrical or vertical.

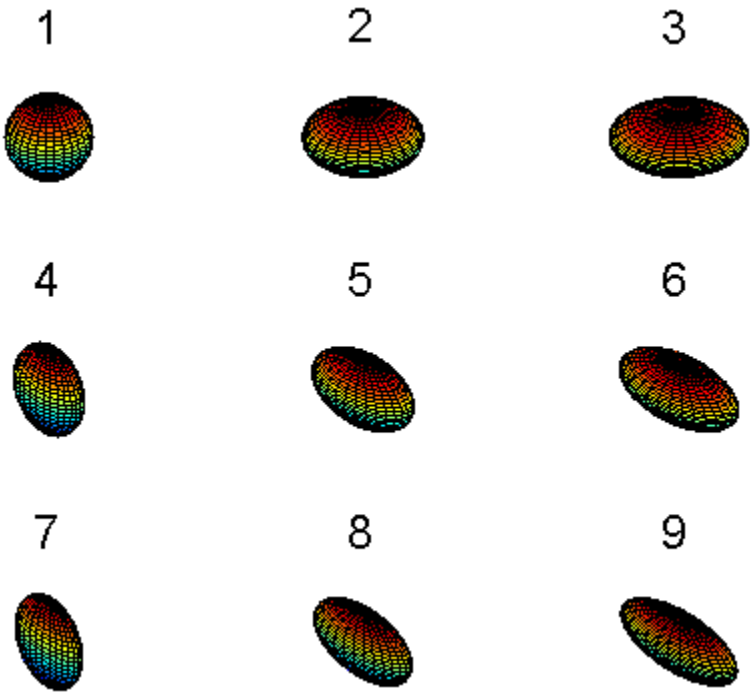

Figure 8: Range of ellipsoidal shapes used to generate far-field displacement waveforms for figure 7 Meq P-wave first motion for Finland EGS controlled stimulation (Kwiatek et al 2019). The mostly likely ellipsoidal shapes are those labelled 5,6,9, indicating a locally lateral distribution of poro-permeability structure.

4, DISCUSSION/CONCLUSIONS

The sustained success of crustal fault-zone seismology detailed by Aki & Richards (2009) has provided an impetus to ascribe an identical physical failure process to microseismicity observed in the ambient crust away from active faults. Missing, however, from the transference of fault-zone failure processes to ambient crust failure processes is the role of crustal fluids.

In failure processes as complex and erratic as fault-zone slip, the role of fluid has been incidental at best and absent at worst. Faults are generically seen to be aspects of distant crustal stress boundaries on quasi-uniform elastic media with little internal structure and little or no connection to fluid content. The planar nature of the stress tensor in quasi-uniform elastic media was, consciously or unconsciously, incorporated into the planar nature of fault slip surfaces. The planar fault-slip mechanics at the crustal scale became anchored in failure processes of lab-scale rock samples described by the Coulomb law of rock friction and applied as stress boundary conditions imposed by rigid steel platens that by St Venant's principle imposed unrealistically uniform internal stress distributions on laboratory samples.

It should not be surprising that EGS stimulation Meqs in the ambient crust brought forth a range of crustal failure processes not covered by Coulomb friction in quasi-uniform elastic media under unrealistically rigid planar stress boundary conditions with no provision for fluids beyond the secondary role of stress relief on incipient or existing failure surfaces. For application to the ambient crust, the assumption of quasi-uniform elastic media is belied by well-log data spatial fluctuation systematic observed throughout the ambient crust. Further, the assumption of fluid irrelevance to failure processes is belied by well-core poroperm data throughout crustal reservoirs also recorded for crystalline basement. Finally, the assumed fault-zone crustal boundary stress conditions are rendered irrelevant for the ambient crust by the presence of spatially correlated poro-permeability distributions that create lognormally distributed and spatially erratic strain response at all scales in the ambient crust. In short, for ambient crust Meq slip processes there is almost no validity to the assumption set that underwrites fault zone slip mechanics.

We show here instead that a minor adjustment to the Stokes/Haskell elastodynamics of (2) and (3) overcomes the contradiction of applying the simplistic assumptions of fault-zone slip mechanics to crustal failure in the ambient crust. In the ambient crust, EGS fluids issuing at controlled pressures/rates form an injection wellbore do not perceive far-field stress uniformity that creates a natural stress-aligned Coulomb failure process along stress-oriented planes in quasi-uniform elastic media. Rather, EGS fluids leak into a pre-existing poro-permeability distribution inherited from the rock-fluid interactions of the rock consolidation processes. Remnants of the generic consolidation processes that result in the poro-permeability fabric $\kappa(x,y,z) \sim \exp(\alpha\varphi(x,y,z))$ observed at all scales from cm to km are seen to force EGS injected fluids along erratic flow channels that include spatially unpredictable clusters of high poro-permeability that accumulate high-pressure fluids injected at the EGS stimulation wellbore. After some time, the accumulated high-pressure fluids breakthrough the confinement of the pre-existing poro-perm cluster to generate a volume distribution of (mostly) radially-directed dislocations that act as Stokes's point forces. This fluid breakout action generates far-field elastic displacements that register on downhole sensors through summation over the terms expressed in (3). The volumetric systematics of the Stokes (mostly) radial dislocations are

then given by the Haskell integral (4). The far-field signature of the volumetric fluid breakout failure processes are seen as the red generic bidirectional displacement waveforms illustrated in Figures 7-8.

Assigning sites of EGS stimulation Meqs to sites of high poro-permeability inherent in the ambient crust fabric $\kappa(x,y,z) \sim \exp(\varphi(x,y,z))$ is at present statistical rather than deterministic. Nor do we know what permanent changes Meq radial flow slip failures make within the over-pressured poro-permeability structures. However, while we do not yet know in advance of stimulation where the high poro-permeability clusters are located in an ambient crust volume, we can project observational circumstances that will yield the relevant information to make at least quasi-deterministic projections of where successive EGS Meqs will occur. And we can logically expect from the rock consolidation origin processes -- i.e., those generating the $\kappa(x,y,z) \sim \exp(\alpha\varphi(x,y,z))$ poro-permeability distributions -- that the poro-connectivity parameter α will increase during EGS stimulation Meq failure. Increasing poro-connectivity parameters α is energetically favourable as increasing permeability does not imply increasing porosity. Increasing porosity works against confining stresses; increasing grain-scale connectivity within existing porosity distributions is inherently less energy-dependent, not least for noting that natural rock consolidation processes eliminate porosity but maintain or increase permeability through systematic incremental increases in poro-connectivity parameter α.

We conclude that EGS stimulation of the ambient crust achieved in Finland and reproduced in the UtahForge project must advance through scientific understanding and accommodation of the crustal poro-permeability empiric $\kappa(x,y,z) \sim \exp(\alpha\varphi(x,y,z))$. This expression derives directly from exhaustively attested well-log/core/flow data and is consistent with current EGS stimulation Meq size and spatial distribution statistics. These statistical data are now validated in detail by Meq far-field waveform empirics showing that Meq source slip distributions are inconsistent with a planar fault-like geometry and are instead straightforwardly consistent with a volumetric surface geometry in line with spatial clustering as found in the $\kappa(x,y,z) \sim \exp(\alpha\varphi(x,y,z))$ poro-permeability empiric.

This data-based conclusion argues against seeking to establish enhanced wellbore-to-wellbore flow structures of arbitrarily large gauge offsets. It is, rather, consistent with small gauge offsets over extensive wellbore reaches. Geothermal resource production can be quantified as wellbore energy flow $Q \sim \rho C \times T \times V$. Wellbore fluid of volume heat capacity is fixed at $\rho C \sim 4.3 MJ/m3 \cdot {}^{o}C$. Prospective temperatures are of order $T \sim 230^{o}C$. In these circumstances, volumetric flow $V \sim 50 L/s$ yields wellbore heat energy production $Q \sim 50 MW_{th}$. Wellbore fluid flow $V = 2\pi r_0 \varphi v_0 \ell$ for open wellbore length ℓ depends on spatially variable product crustal porosity times crustal fluid velocity $v \equiv \varphi v_0$ at wellbore radius r_0. Of the deciding variables for geothermal output Q, only ℓ is within ready control. Significantly increasing wellbore inflow $v \equiv \varphi v_0$ through enhancing local inter-wellbore flow rates v_0 requires engineering technology that has not yet fully grappled with the poro-permeability structure of the ambient crust. It is safe to say, however, that in light of the reality of ambient crust poro-permeability distributions, wellbore-pair offsets should not pre-empt the need for secure scientific investigation defined by and expanded beyond the new Meq empirics that are firmly established in the background empirics of ambient crust well-log/core/flow data.

REFERENCES

Aki, K, and P. Richards Quantitative Seismology, 2nd Edition University Science Books ISBN-10. 1891389637 · ISBN-13. 978-1891389634· Publication date. March 25, 2009

Haskell, N.A., 1963, Radiation pattern of Rayleigh waves from fault of arbitrary dip and direction of motion in a homogeneous medium, Bull. Seisin. Soc. Am., 53, 619-642.

Haskell, N.A., 1964a, Radiation pattern of Rayleigh waves from point sources in a multilayered medium, Bull. Seisin. Soc. Am., 5d, 377-393.

Haskell, N.A., 1964b, Total energy and energy spectral density of elastic wave radiation from propagating faults, Bull. Seisin. Soc. Am., 5d, 1811-1841.

Haskell, N.A., 1966, Total energy and energy spectral density of elastic wave radi- ation from propagating faults. Part II. A statistical model, Bull. Seisin. Soc. Am., 56, 125-140.

Haskell, N.A., 1969, Elastic displacements in the near-field of a propagating fault, Bull. Seisin. Soc. Am., 59, 865-908.

Kwiatek, G., T. Saarno, T. Ader, F. Bluemle, M. Bohnhoff, M. Chendorain, G. Dresen, P. Heikkinen, I. Kukkonen, P. Leary, M. Leonhardt, P. Malin, P. Martínez-Garzón, K. Passmore, P. Passmore, S. Valenzuela, C. Wollin, Controlling fluid-induced seismicity during a 6.1-km-deep geothermal stimulation in Finland. Sci. Adv. 5, eaav7224 (2019).

Lay, T., and T. C. Wallace (1995). Modern Global Seismology, Academic Press, San Diego, 521pp.

Verma, A., and Pruess, K.: Enhancement of Steam Phase Relative Permeability Due to Phase Transformation Effects in Porous Media, Proceedings, 11th Workshop on Geothermal Reservoir Engineering, Stanford University, Stanford, CA (1986). <Reference Style>

Wang, C.T., and Horne, R.N.: Boiling Flow in a Horizontal Fracture, Geothermics, 29, (1999), 759-772. <Reference Style>

APPENDIX A -- WELL-LOG/CORE/FLOW DATA YIELDING AMBIENT CRUST PORO-PERMEABILITY EMPIRIC $\kappa \sim \exp(\alpha\varphi)$

The fluid flow material properties of ambient crustal rock are set by a trio of widely attested empirical field relations (i)-(iii) derived respectively from crustal well-log, well-core, and well-productivity data. Closely associated with these crustal poroperm statistical and spatial distribution empirics are microseismic event empirics (iv)-(vi) observed in crystalline basement, geothermal fields, and active deformation zones.

(i) Well-log spatial sequences of rock properties establish the existence of long-range power-law-scaling spatial correlations as a fundamental feature of the ambient brittle-fractured crust. Well-log Fourier power-spectra, $S(k) \propto 1/k^{\beta}$, $\beta \sim 1$, span five decades of spatial frequency, $1/\text{cm} < k < 1/\text{km}$ [A1-A2]. Random number fields with power-law scaling spectral power exponent $\beta \sim 1$ are termed "pink noise". Of particular interest are neutron porosity logs from hydrocarbon reservoirs, geothermal formations, and basement rock at up to 6km depth. For contrast, the de facto standard assumption about crustal heterogeneity is lack of significant spatial correlation termed ''white noise'' with $\beta = 0$ power-spectra, $S(k) \propto 1/k^0 \sim$ const. There are virtually no examples of "white noise" well-log fluctuations other than when weak physical signals reduce to recorder background noise.

(ii) Well-core data from hydrocarbon reservoirs, geothermal formations, and deep basement rock show close spatial correlation systematics, $\delta\log\kappa \sim \alpha\delta\varphi$, for spatially varying porosity φ and permeability κ [A3-A4]. On well-core evidence, rock permeability is a physical feature of fracture-connectivity between spatially-correlated porosity structures at all scales. The constant α in the well-core poroperm spatial correlation is given by the empiric condition $\alpha\underline{\varphi} \sim 3\text{-}5$ across two decades of mean porosity, $0.3\% < \underline{\varphi} < 30\%$ spanning the basement-to-reservoir formation spectrum [A5-A6]. The well-core empiric for porosity and permeability follows from considering that connectivity between n pores scales as n-factorial, $n! = n(n-1)(n-2)\ldots 1$, so that changes in pore count $n \rightarrow n+\delta n$ lead to changes in the logarithm of permeability $\delta\log n! \sim \log((n+\delta n)!) - \log(n!) \sim \delta n \log(n)$, giving the observed well-log poroperm relation. The constant of proportionality α governs the degree to which pores are connected, with high degree of pore connectivity leading to channelised flow structures.

(iii) Well-productivity lognormality follows directly from the integrated poroperm relation $\kappa \sim \kappa_0 \exp(\alpha\varphi)$. The empirical condition $\alpha\underline{\varphi} \sim 3\text{-}5$ guarantees the lognormal well-productivity distributions observed everywhere for groundwater aquifers, conventional and unconventional hydrocarbon reservoirs, convective geothermal systems, and mineral deposition abundances in fossil flow systems [A7-A8].

(iv) Ambient crust microseismicity event magnitude distributions in the magnitude range $-1 < m < 2$ are lognormal rather than power-law/fractal, i.e., the standard Gutenberg-Richter relation [A9-A10]. The observed lognormal magnitude distribution is congruent with crustal permeability lognormality (iii), indicating that ambient crustal microseismic slip events are closely associated with crustal permeability structures.

(v) Volume distributions of ambient crust permeability and microseismic event separations are spatially correlated according to two-point spatial correlation function $\Gamma(r) \sim 1/r$ [11-12]; in 2D sections of volume distribution the two-point correlation function reduces to $\Gamma(r) \sim 1/r^{1/2}$. The similar spatial correlation functions and scaling exponents indicate that microseismic slip events tend to occur on permeability structures rather than hypothetical fault structures.

[A1] Leary PC (2002) Fractures and physical heterogeneity in crustal rock, in Heterogeneity in the Crust and Upper Mantle: Nature, Scaling, and Seismic Properties, J. A. Goff and K. Holliger, Eds., pp. 155–186, Kluwer Academic/Plenum Publishers, New York, NY, USA, 2002.

[A2] Leary P, Malin P & Niemi R (2017) Fluid flow & heat transport computation for power-law scaling poroperm media, Geofluids, Volume 2017, https://doi.org/10.1155/2017/9687325

[A3] Leary P, Malin P, Saarno T, Kukkonen I (2018) $\alpha\varphi \sim \alpha\varphi_{crit}$ - Basement rock EGS as extension of reservoir rock flow processes. Proceedings 43th Workshop on Geothermal Reservoir Engineering, Stanford University, February 12-14

[A4] Malin PE, Leary PC, Cathles LM and Barton CC, Observational and Critical State Physics Descriptions of Long-Range Flow Structures Geosciences 2020, 10, 50; doi:10.3390/geosciences10020050

[A5] Leary P, Malin P, Pogacnik J, Rugis J, Valles B & Geiser P (2014) Lognormality, dk ~ kdf, EGS, and all that, Proceedings 39th Stanford Geothermal Workshop, February 24-26 2014, Stanford University, CA.

[A6] Leary P, Malin P, Saarno T & Kukkonen I (2017) Prospects for Assessing Enhanced Geothermal System (EGS) Basement Rock Flow Stimulation by Wellbore Temperature Data, Energies, vol 10, no. 12, DOI: 10.3390/en10121979.

[A7] IFC (2013) Success of geothermal wells: A global study, international finance corporation. International Finance Corporation. 2013. Available from: https://www.ifc.org/wps/wcm/connect/topics_ext_content/ifc_external_corporate_site/sustainability-at-ifc/publications/publications_gpn_geothermal-wells.

[A8] Malin P, Leary P, Shalev E, Rugis J, Valles B, Boese C, Andrews J & Geiser P (2015) Flow Lognormality and Spatial Correlation in Crustal Reservoirs: II – Where-to-Drill Guidance via Acoustic/Seismic Imaging, WGC2015, 19-24 April, Melbourne AU

[A9] Leary P, Malin P & Saarno T (2020) A Physical Basis for the Gutenberg-Richter Fractal Scaling, 45th Workshop on Geothermal Reservoir Engineering, Stanford University, February 10-12, SGP-TR-216 1.

[A10] Zaky DA, Nugraha AD, Sule R & Jousset P (2015) Spatial analysis of earthquake frequency-magnitude distribution at geothermal region in the south of Bandung, West Java, Indonesia, 9th International Workshop on Statistical Seismology, 14-18 June, Potsdam, Germany

[A11] Leary P, Malin P, Saarno T, Heikkinen P, Diningrat W (2019) Coupling crustal seismicity to crustal permeability - Power-law spatial correlation for EGS-induced and hydrothermal seismicity. Proceedings of the 44th Workshop on Geothermal Reservoir Engineering, Stanford University, February 11-13.

[A12] Leary P & Malin P (2020) Correlation function $\Gamma_{meq}(r) \sim 1/r^{1/2}$ coupling of microseismicity to permeability -- The basis for fluid flow seismic image targeting for geothermal production wells, Proceedings World Geothermal Congress 2021 Reykjavik, Iceland, 21-26 May 2021.

APPENDIX B -- MICROSEISMICITY CORNER FREQUENCY SCALING AND STRESS RELEASE

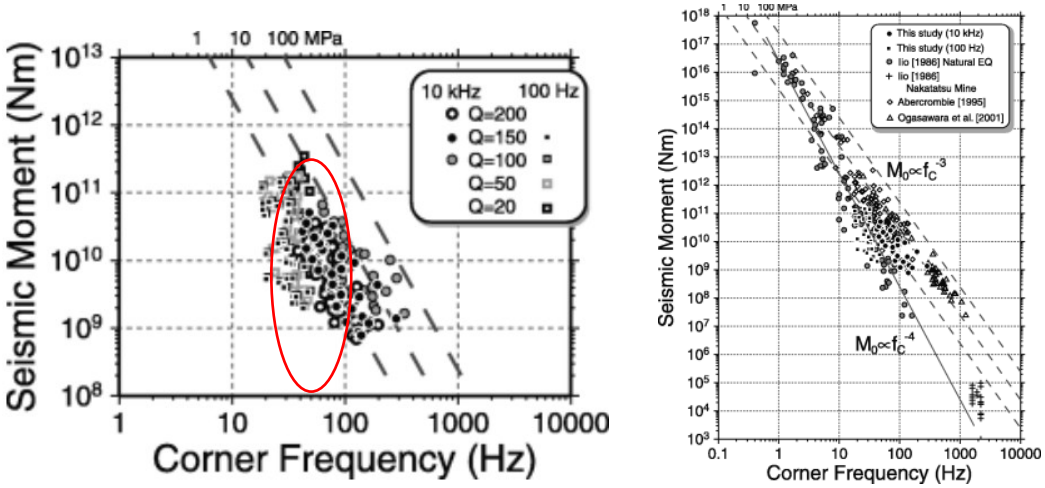

10^9 N-m = 10^{16} dyne-cm → Mw = 2/3 16 - 10.7 = 10 – 10.7 ~ 0 → 100Hz corner frequency

10^{10} N-m = 10^{18} dyne-cm → Mw = 2/3 17 - 10.7 = 12 – 10.7 = 0.6 → 10Hz corner frequency

Hiramatsu Y, Yamanaka H, Tadokoro K, Nishigami K & Ohmi S (2002) Scaling law between corner frequency and seismic moment of microearthquakes: Is the breakdown of the cube law a nature of earthquakes? https://doi.org/10.1029/2001GL013894

APPENDIX C – MEQ SIZE/SPATIAL-CORRELATION DISTRIBUTIONS FOR FINNISH BASEMENT EGS STIMULATION

As given in Appendix A, crustal rock-fluid interaction empirics from well-log, well-core, and well-flow data worldwide define ambient crust spatially correlated poro-permeability structures $\kappa(x,y,z) \sim \exp(\alpha\varphi(x,y,z))$ at scales from cm to km. Finnish EGS Meqs show that lognormally distributed poro-permeability structures correlate with sites of EGS stimulation Meq strain energy release that occurs via slow erratic slip processes instead of rapid slip along quasi-uniform planar faults.

The 2018 controlled EGS fluid injection stimulation at 6km depth in Finnish crystalline basement produced some 2655 Meqs across the (estimated) magnitude range $-1.5 < m_{est} < 2$ within in a 5-km-scale crustal volume as shown in Figure C1 (left). Of these Meq events, some 2176 events were proximate to the deviated injection wellbore interval below 5.5km as in Figure 1 (right). Figure C2 vertically sections these latter events into four horizontal arrays of 500m thickness and 2x4 km lateral extent; the array sections have event populations 531, 507, 912 and 226 respectively.

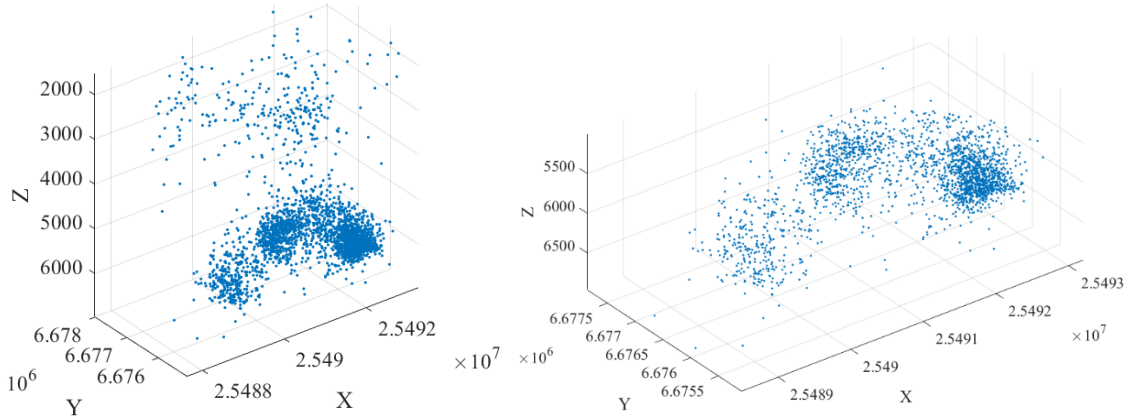

Figure C1 – (Left) Full volume crustal array of Finnish basement EGS stimulation Meq locations. (Right) Expanded array of left-hand lower crustal Meq event locations.

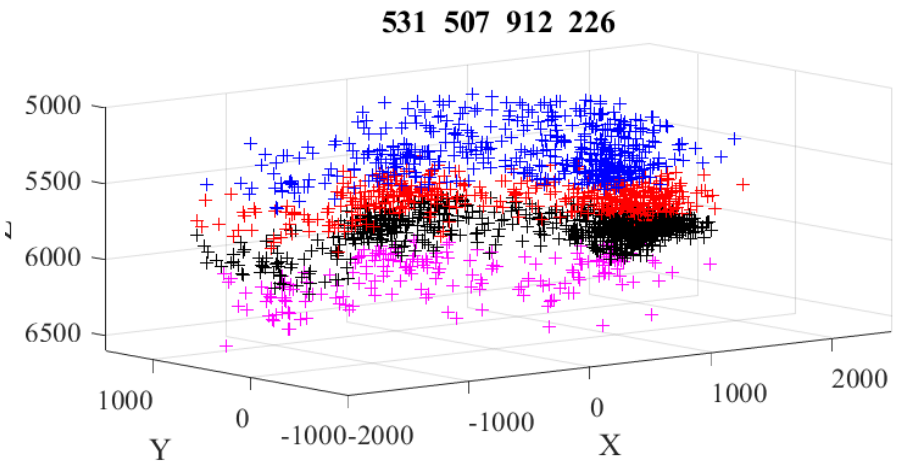

Figure C2 – Four level section arrays of Finnish basement EGS stimulation Meq locations (section event numbers given in plot title).

The frequency distributions of the Figure C2 section event moments are seen in Figure C3 as fit to lognormal distributions numerical realised for ambient crust empirical poro-permeability relation $\kappa(x,y,z) \sim \exp(\alpha\varphi(x,y,z))$. The curve realisations assume a normal porosity distribution of mean value $\underline{\varphi} = 20\%$ with 5% standard deviation for the given values of the poro-connectivity fit parameter α. Well-core and well-flow empirics for reservoir formations worldwide establish a parameter constraint relation $\sim 3 < \alpha\underline{\varphi} < \sim 5$ for α. The Figure C3 numerical realisation condition $\alpha\underline{\varphi} \sim 4\text{-}5$ meets the crustal reservoir constraint as might be expected for crystalline basement rock whose well-log, well-core and well-flow spatial correlations accord with ambient crustal empirics at large.

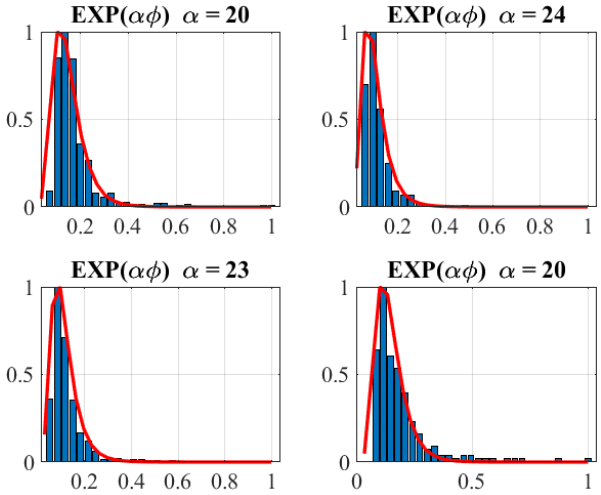

Figure C3 – Normalised event moment lognormal frequency distributions for Figure C2 Meq section arrays of Finnish basement EGS stimulation. Red curve lognormal fits derive from ambient crust poro-permeability relation $\kappa(x,y,z) \sim \exp(\alpha\varphi(x,y,z))$.

It is well established that the Finnish EGS Meq magnitude range is "complete". Figure C3 thus equally well establishes that ambient crust Meq moment distributions are lognormal rather than fractal/power-law. Expectations of an indefinitely large number of small Meqs as predicted by the Gutenberg-Richter fractal relation derived from fault zone seismicity are not met by ambient crust Meq activity.

The Figure C3 empirical/physical restatement of the Gutenberg-Richter relation for ambient crust Meqs as lognormal crustal poro-permeability event populations given by $\kappa(x,y,z) \sim \exp(\alpha\varphi(x,y,z))$ opens the door for wider understanding of EGS ambient crust stimulation. The Finnish EGS stimulation Meq spatial location data of Figures C4-C6 illustrate the spatial correlation feature of crustal permeability in terms of two-point spatial correlation of Meq events.

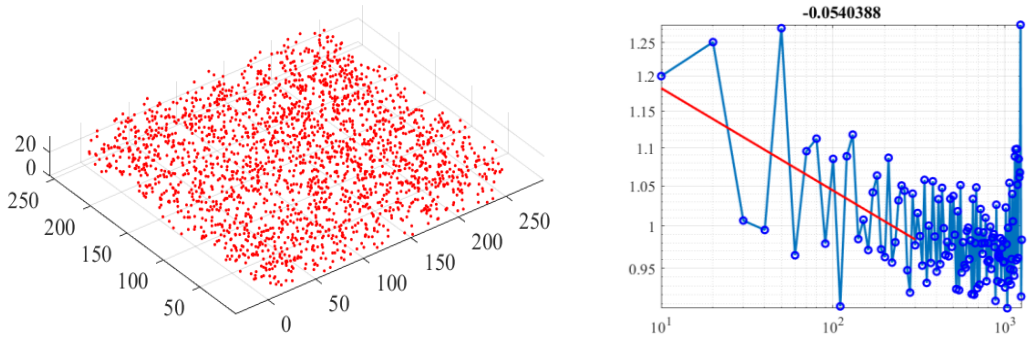

Figure C4 – (Left) Section array of spatially uncorrelated (white noise) high permeability location points. (Right) Array point spatial correlation function $\Gamma(r) \sim 1/r^p$, $p \sim 0$.

Uncorrelated randomness has been the default assumption for generic crustal fracture studies. If we suppose that ambient crust random distributions of porosity are uncorrelated, then numerical realisations of $\kappa(x,y,z) \sim \exp(\alpha\varphi(x,y,z))$ generate spatial distributions of high-value permeability as seen in Figure C4 (left). Applying the two-point pair-wise spatial correlation as a function of event-pair offset r gives the result shown in Figure C4 (right), $\Gamma(r) \sim 1/r^p$ with exponent $p \sim 0$.

Knowing from Figure C3 lognormality that crustal poro-permeability distributions cannot be uncorrelated, we quantify correlations through ambient crust well-log spatial correlation empirics. Figure C5 shows numerically evaluated $\kappa(x,y,z) \sim \exp(\alpha\varphi(x,y,z))$ permeability spatial distributions for spatially correlated, i.e. pink noise, porosity $\varphi(x,y,z)$. The resultant permeability distribution in Figure C5 (left) yields two-point spatial correlation functions with significant exponent values, $\Gamma(r) \sim 1/r^p$, $p \sim 0.74$ as in Fig 5 (right). Figure C6 quantifies the $\Gamma(r) \sim 1/r^p$, $p \sim 1$, two-point spatial correlation property of the Finnish basement controlled EGS stimulation Meqs.

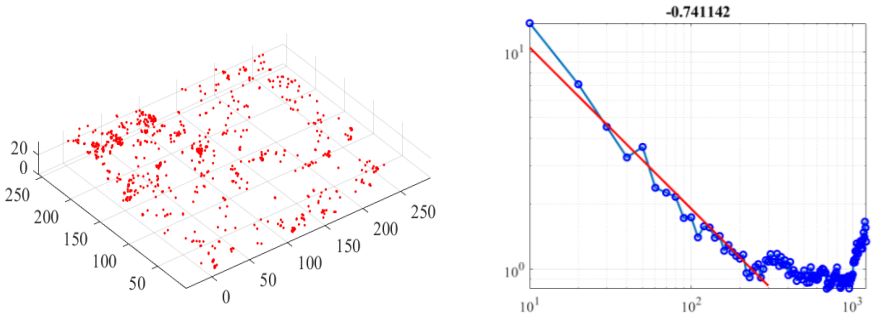

Figure C5 – (Left) Section array of spatially correlated (pink noise) high-permeability locations points. (Right) Array point spatial correlation function $\Gamma(r) \sim 1/r^p$, $p \sim 0.74$.

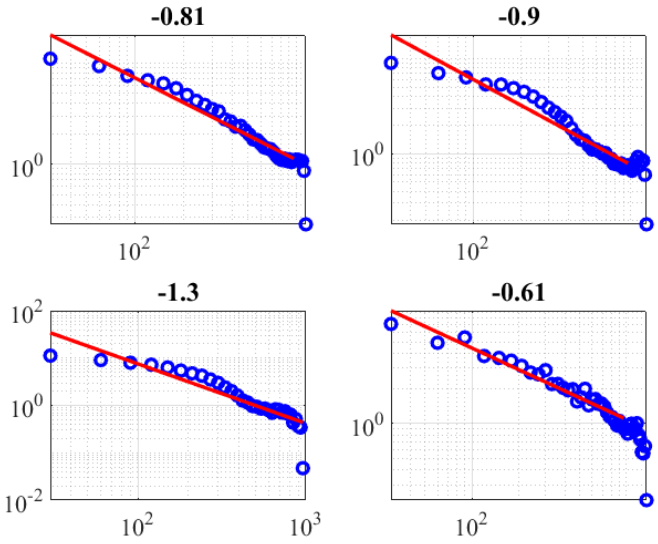

Figure C6 – Spatial correlation functions $\Gamma(r) \sim 1/r^p$ for Figure C2 section level arrays, $p \sim [0.8\ 0.9\ 1.3\ 0.6]$